L^2 Sampled Signal Reconstruction With Causality Constraints–Part I: Setup and Solutions

Gjerrit Meinsma and Leonid Mirkin, *Member, IEEE*

***Abstract*—This paper studies the problem of reconstructing an analog signal from its sampled measurements, in which the sampler (acquisition device) is given and the reconstructor (interpolator/hold) is the design parameter. We formulate this problem as an L^2 (Wiener/Kalman filtering like) optimization problem and place the main emphasis on a systematic incorporation of *causality constraints* into the design procedure. Specifically, the optimization problem is solved under the constraint that the interpolation kernel is l-causal for a given $l \in \mathbb{N}$, i.e., that its impulse response is zero in the time interval $(-\infty, -lh)$, where h is the sampling period. We present a closed-form state-space solution of the problem, whose computational complexity does not depend on l and which can be efficiently calculated and implemented.**

***Index Terms*—Causality, mean-square optimization, model matching, sampling and reconstruction.**

I. Introduction

In these two papers, we study the problem of reconstructing analog signals from their given sampled measurements. The problem is presented in Fig. 1. Here, $\mathcal{S}$ is a given, possibly non-ideal, sampling (acquisition) device, which generates a discrete measurement $\bar{y}$ from an analog signal v. Our goal is to design a reconstructor, containing a discrete filter $\bar{\mathcal{F}}$ and an interpolator (hold device) $\mathcal{H}$, which produces an accurate reconstruction u of v. The separation of the reconstructor to a discrete part and an interpolator is not essential, and without loss of generality we may assume that $\bar{\mathcal{F}}$ is the identity. It, however, might be convenient from the implementation point of view and in the discussion below. We assume that $\bar{\mathcal{F}}$ and $\mathcal{H}$ are linear and shift invariant, which means that we consider reconstruction devices $\mathcal{H}\bar{\mathcal{F}}$ of the form

$$u(t) = \sum_{i \in \mathbb{Z}} \phi(t - ih)\bar{y}[i], \quad t \in \mathbb{R} \tag{1}$$

where $\phi(t)$ is an *interpolation kernel* or *hold function* to be found and $h > 0$ is a given sampling period.

The reconstruction problem has been extensively studied in the literature. If v is bandlimited and $\mathcal{S}$ is the ideal sampler, the sampling theorem [1]–[3] states that v can be perfectly reconstructed, provided the bandwidth of v does not exceed the Nyquist frequency $\omega_{\mathrm{N}} := \pi/h$. The perfect reconstruction is then delivered by the reconstructor with the sinc-interpolation kernel $\phi(t) = \mathrm{sinc}_h(t) := \sin(\omega_{\mathrm{N}}t)/(\omega_{\mathrm{N}}t)$. Perfect reconstruction is possible for some other classes of analog signals; see, e.g., [4], in which cases ϕ can be determined from properties of v. Frequently, however, v cannot be perfectly reconstructed, so weaker requirements on u, like optimality or consistency, are considered. For example, the sinc-interpolator can still be justified if v has dominant low frequencies and $\mathcal{S}$ involves prefiltering v with the ideal lowpass filter, in which case the sinc-interpolator is both L^2 (mean-square) [2] and L^∞ (minmax) [5] optimal. If $\mathcal{H}$ is fixed, the discrete filter $\bar{\mathcal{F}}$ can be designed to minimize various optimality criteria, like mean-square or min-max [6], or to guarantee the consistency of reconstruction in the sense that $\mathcal{S}u = \bar{y}$ for all admissible v [2]. Frequently used choices for $\mathcal{H}$ in the latter case are polynomial B-splines, resulting in cardinal B-splines [7] as interpolation kernels $\phi(t)$. In some optimization formulations $\mathcal{H}$ can be designed too [8]. A unified setup, within which many of these results, from the sinc-interpolator to cardinal splines, can be produced as solutions to norm-optimization problems, was studied in [5].

A common attribute of these solutions is that they do not take into consideration any *causality requirement* on the designed reconstructors. As a result, the available reconstruction methods normally produce noncausal solutions: to reconstruct $v(t)$ at any time instance t we have to know the whole time history, both in the past and in the future, of $\bar{y}$. Yet in many online applications only a finite preview of $\bar{y}$, if any, is available. This problem is commonly resolved by the truncation of a noncausal part of $\phi(t)$, after it is designed. This is thoroughly exposed in [9], which also contains many relevant references. This approach, however, is ad hoc and can only be justified if the truncated part is insignificant, which, in turn, requires sufficiently fast decay of a noncausal part of $\phi(t)$. For example, this approach works poorly for the sinc-reconstructor as $\mathrm{sinc}_h(t)$ has slow decay.[1] This is why the decay rate is an important factor in the choice of $\mathcal{H}$; see [2, p. 572]. However, the fast decay requirement might compromise the reconstruction performance.

In this paper, we put forward a different idea. We cast the reconstruction problem as a mean-square optimization problem for the whole, hybrid, reconstructor and enforce the following relaxed causality requirement:

$$\phi(t) = 0, \quad \text{whenever } t < -lh \tag{2}$$

[1]In fact, we shall show in Appendix B that reconstructors with one-side truncated sinc interpolation kernels are even not L^2-stable.

Manuscript received November 22, 2010; revised April 22, 2011 and November 02, 2011; accepted January 10, 2012. Date of publication January 23, 2012; date of current version April 13, 2012. The associate editor coordinating the review of this manuscript and approving it for publication was Prof. Trac D. Tran. This research was supported by the Israel Science Foundation (Grant 1238/08).

G. Meinsma is with the Department of Applied Mathematics, University of Twente, 7500 AE Enschede, The Netherlands (e-mail: g.meinsma@utwente.nl).

L. Mirkin is with the Faculty of Mechanical Engineering, Technion—Israel Institute of Technology, Haifa 32000, Israel (e-mail: mirkin@technion.ac.il).

Color versions of one or more of the figures in this paper are available online at http://ieeexplore.ieee.org.

Digital Object Identifier 10.1109/TSP.2012.2185228

1053-587X/$31.00 © 2012 IEEE

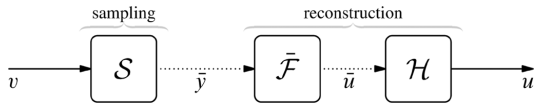

Fig. 1. Sampling and reconstruction setup.

for a given $l \in \mathbb{Z}^+$ called the *smoothing lag*, as a hard constraint on this optimization procedure. Toward this end, we follow the system-theoretic approach in which signals are modeled through their generating systems and performance requirements are expressed in terms of system norms [10], [11]. In the terminology of [5], we consider the Type-III (fixed sampler, free reconstructor) L^2 (Wiener/Kalman) problem.

If no causality constraints are imposed, this optimization produces known cardinal polynomial or exponential splines, depending on the choice of the model of v [5]. Optimal solutions minimizing the very same performance index, yet with causality constraints imposed, may therefore be regarded as *causal cardinal splines*. Having the smoothing lag as a part of the optimization process has a clear advantage over ad hoc truncations of noncausal solutions. We no longer hinge on the decay rate of $\phi(t)$ and can therefore use a wider class of signal generators and, consequently, a richer set of reconstructors. Moreover, the optimization-based design makes it easy to link preview with the achievable performance, which may be useful in justifying the choice of the preview length l.

The incorporation of causality requirements nontrivially changes the solution procedure. Optimization problems without causality constraints are essentially static in the frequency domain, i.e., we may design the reconstructor independently at each frequency. This is no longer possible when causality constraints are imposed because of analyticity requirements [11]. Different, more involved, techniques are then requisite. In the case of $l = 0$, referred to as the L^2 filtering, the solution is well-known in the literature [12] and can be traced back to [13] (see also [14] for a closed-form L^∞ filtering solution). The case of $l > 0$, referred to as the fixed-lag smoothing, is more challenging and less studied in the sampled-data context. If only the discrete filter $\bar{\mathcal{F}}$ is the design parameter, the problem can in principle be converted to an equivalent filtering problem by augmenting a discretized signal generator with the delay z^{-l} as described in [10], [15]. This, approach, however, produces nontransparent and numerically inefficient (dimensions inflate with l) solutions, which cannot address important questions of the rationale, structure, and interpretations of causal reconstructors, see the discussion in [15, Sec. III]. This approach also is not readily extendible to the design of the interpolator $\mathcal{H}$.

In this paper we derive a closed-form solution to the L^2 reconstruction problem for an arbitrary smoothing lag l. This solution is based on one Riccati and one Lyapunov matrix equations and can be efficiently computed and implemented using state-space methods. The equations above do not depend on l, which is evidently advantageous over augmentation-based approaches. Our approach also allows one to incorporate steady-state behavior constraints via the use of unstable signal generators. A conference version of this paper was presented at the 2006 IEEE ICASSP; see [16].

To streamline the exposition, we have divided the presentation into two parts. In the first part, the problem is formulated and the solution is presented without proofs. Part II of this paper [17] presents technical developments that are relevant for the problems under consideration, but also have independent interest. This part is organized as follows. In Section II, the optimization problem we address is formulated. The solution, which is the main result of this paper, is then formulated in Section III. Frequency-domain properties of the optimal solution are discussed in Section IV. As an example illustrating the proposed approach, we then consider the design of causal cubic splines in Section V. Concluding remarks are provided in Section VI. Finally, Appendix A collects short technical derivations, which do not rely on the lifting technique, and in Appendix B, we show that the reconstructor with a one-side truncated sinc as its interpolation kernel is L^2-unstable.

Notation

Throughout both parts signals are represented by lowercase symbols such as $y(t) : \mathbb{R} \to \mathbb{C}$ and overbars indicate discrete time signals, $\bar{y}[k] : \mathbb{Z} \to \mathbb{C}$. For a set $\mathbb{A}$, the indicator function $\mathbb{1}_{\mathbb{A}}(t)$ is 1 if $t \in \mathbb{A}$ and 0 elsewhere. By n_v we understand the number of elements of a vector-valued signal v. The notation M' is used for the transpose of a matrix M. Uppercase calligraphic symbols, like $\mathcal{G}$, denote continuous-time systems in the time domain. Corresponding transfer functions/frequency responses are then presented by uppercase symbols, like $G(s)$ and $G(\mathrm{j}\omega)$. Discrete-time systems, transfer functions, etc., are denoted by overbars, like $\bar{\mathcal{G}}$, $\bar{G}(z)$, etc.

By $\mathbb{Z}_l^+$, we denote the set of all integers larger or equal to l and then $\mathbb{Z}_l^- := \mathbb{Z} \setminus \mathbb{Z}_l^+$ is the set of integers smaller than l. The symbols $\mathbb{T}$, $\mathbb{D}$, and $\bar{\mathbb{D}}$ stand for the unit circle ($|z| = 1$), the open unit disk ($|z| < 1$), and the closed unit disk ($|z| \leq 1$) in the complex plane, respectively.

II. Problem Formulation

To pose the reconstruction problem formally, we supplement the scheme in Fig. 1 with a few extra ingredients as shown in Fig. 2. Here

$$\mathcal{G} = \begin{bmatrix} \mathcal{G}_v \\ \mathcal{G}_y \end{bmatrix}$$

is an LTI system, embodying our information about properties of the reconstructed signal v, the sampled signal y (not necessarily different from v), and their dependencies. The constant matrix $\Sigma \geq 0$ is the covariance matrix of the measurement noise $\bar{n}$, reflecting imperfections of the sampling process, like quantization errors [18]. The signals w_v and $\bar{w}_n$ are fictitious normalized signals, which generate the "physical" signals v, y, and $\bar{n}$. The reconstruction error $e := v - u$ reflects the closeness of the reconstruction u to v.

We say that a reconstructor $\mathcal{H}\bar{\mathcal{F}}$ is *admissible* if it is of the form (1) and stable, in the sense that it is bounded as an operator $\ell^2(\mathbb{Z}) \to L^2(\mathbb{R})$. This stability requirement does not mean to limit $\bar{y}$ to be an $\ell^2(\mathbb{Z})$ signal, but rather to guarantee that the reconstructed signal u does not blow up. Also, $\mathcal{H}\bar{\mathcal{F}}$ is said to be

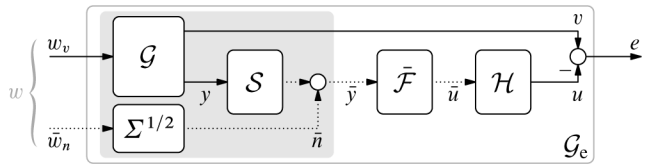

Fig. 2. The problem setup.

l-causal if its interpolation kernel $\phi(t)$ satisfies (2). The reconstruction problem is then cast as the following L^2 optimization for the setup in Fig. 2:

RP$_l$ Let a finite-dimensional system $\mathcal{G}$, a matrix $\Sigma \geq 0$, and $l \in \mathbb{Z}_0^+$ be given and let $\mathcal{S}$ be the ideal sampler. Find an admissible and l-causal reconstructor $\mathcal{F}_l = \mathcal{H}\bar{\mathcal{F}}$, which stabilizes the error system

$$\mathcal{G}_{\mathrm{e}} := [\,\mathcal{G}_v 0\,] - \mathcal{H}\bar{\mathcal{F}}[\mathcal{S}\mathcal{G}_y \quad \Sigma^{1/2}] \tag{3}$$

and minimizes its L^2 system norm, $\|\mathcal{G}_{\mathrm{e}}\|_2$, over all admissible and l-causal reconstructors.

The remainder of this section is devoted to explanations of some aspects of this formulation (for more details, see [11]). In particular, we comment on the use of the signal generator $\mathcal{G}$ to model v and y, motivate the use of unstable generators, and discuss the L^2 system norm.

A. System-Based Modeling

In accordance with the system-theoretic approach, we express the available information about v, $\bar{y}$, and their relations via modeling these signals as outputs of the *signal generator* (shown by the gray box in Fig. 2), driven by a common normalized signal $w = \begin{bmatrix} w_v \\ \bar{w}_n \end{bmatrix}$. While the modeling of $\bar{n}$ as a white noise is standard [6], [8], the use of dynamical systems in representing signals of interest is less common in sampling and reconstruction problems. We therefore present below several examples, illustrating the construction of $\mathcal{G}$.

Let v and y be stochastic processes with power spectral densities (PSD) $\Phi_v(\omega)$ and $\Phi_y(\omega)$ and a cross-spectral density $\Phi_{yv}(\omega) = [\Phi_{vy}(\omega)]^*$. This is equivalent [19, Sec. 6.4] to presenting v and y as the outputs of a system $\mathcal{G}$, whose frequency response $G(\mathrm{j}\omega)$ verifies

$$G(\mathrm{j}\omega)[G(\mathrm{j}\omega)]^* = \begin{bmatrix} \Phi_v(\omega) & \Phi_{vy}(\omega) \\ \Phi_{yv}(\omega) & \Phi_y(\omega) \end{bmatrix} \geq 0,$$

driven by a standard white noise process w_v (standard means having unit spectral density). Thus, the signal generator in this case is a fictitious system, reflecting our knowledge of properties of v and y. In fact, without loss of generality we can assume in this case that $\mathcal{G}$ is causal.

The signal generator does not have to be completely fictitious. For example, let v have the PSD $\Phi_v(\omega)$ and assume that y is v, measured by a sensor with the transfer function $F_{\mathrm{s}}(s)$ and corrupted by an analog noise, which is independent of v and has the PSD $\Phi_n(\omega)$. In this case, $\mathcal{G}$ is a system with the transfer function

$$G(s) = \begin{bmatrix} G_v(s) & 0 \\ F_{\mathrm{s}}(s)G_v(s) & G_n(s) \end{bmatrix} \tag{4}$$

where $\mathcal{G}_v$ and $\mathcal{G}_n$ are any (causal) systems, whose frequency responses satisfy $|G_v(\mathrm{j}\omega)|^2 = \Phi_v(\omega)$ and $|G_n(\mathrm{j}\omega)|^2 = \Phi_n(\omega)$, and w_v is again standard white noise.

The system-based modeling also suits deterministic, or even mixed deterministic/stochastic, problems. For example, the generator in (4) can reflect the situation, when v is a low-pass signal with the baseband frequency ω_{b}. We then may choose $\mathcal{G}_v$ as a low-pass filter with the bandwidth ω_{b}. In this case, w_v is comprised of both a deterministic normalized broadband component (generating v) and a white noise (generating the measurement noise).

B. Stability of the Error System

The error system $\mathcal{G}_{\mathrm{e}}$ defined by (3) is a linear map from $w = \begin{bmatrix} w_v \\ \bar{w}_n \end{bmatrix}$ to e. By the stability of $\mathcal{G}_{\mathrm{e}}$ we understand that it is a *bounded operator* $L^2(\mathbb{R}) \times \ell^2(\mathbb{Z}) \to L^2(\mathbb{R})$. If the signal generator $\mathcal{G}$ is itself stable, the error system is stable whenever so is the reconstructor. In other words, in this case the stability requirement on $\mathcal{G}_{\mathrm{e}}$ is redundant. There are situations, however, when it might be required to include unstable dynamics into $\mathcal{G}$. In such situations, the stability requirement imposes additional constraints on the reconstructor.

Our primary motivation for allowing unstable $\mathcal{G}$ is the use of signal generators with $\mathrm{j}\omega$-axis poles to impose steady-state requirements. To explain the idea, consider a simple analog deconvolution problem, where a signal v is recovered from its noise-free measurement $y = \mathcal{F}_{\mathrm{s}}v$ by a deconvolution filter $\mathcal{F}_{\mathrm{d}}$. To guarantee perfect steady-state recovery of a constant v (*unbiased* deconvolution), we have to assure that the static gain of $\mathcal{F}_{\mathrm{d}}$ satisfies the interpolation constraint $F_{\mathrm{d}}(0) = 1/F_{\mathrm{s}}(0)$. In terms of the error system $\mathcal{G}_{\mathrm{e}} = 1 - \mathcal{F}_{\mathrm{d}}\mathcal{F}_{\mathrm{s}}$, this constraint reads $G_{\mathrm{e}}(0) = 0$. A key observation is that the latter condition is equivalent to the stability of the transfer function $\tilde{G}_{\mathrm{e}}(s) := G_{\mathrm{e}}(s)\frac{s+a}{s}$ for any $a > 0$. Indeed, if we assume that $\mathcal{F}_{\mathrm{s}}$ and $\mathcal{F}_{\mathrm{d}}$ are stable, the pole at the origin is the only source of instability in $\tilde{G}_{\mathrm{e}}(s)$. Hence, $\tilde{G}_{\mathrm{e}}(s)$ is stable iff $G_{\mathrm{e}}(s)$ cancels this pole, which, in turn, is equivalent to the zero static gain of $G_{\mathrm{e}}(s)$. Thus, the interpolation constraint $F_{\mathrm{d}}(0) = 1/F_{\mathrm{s}}(0)$ can be imposed through incorporating a pole at the origin into the model of v.

The reasonings above extend straightforwardly to situations where asymptotically perfect recovery of a ramp (double pole at the origin), a sine wave with the frequency ω_0 (poles at $\pm\mathrm{j}\omega_0$), etc., is required and to more general problems. Casting interpolation constraints as a stabilization problem facilitates extensions to non time-invariant problems, like the signal reconstruction studied here.

C. L^2 System Norm

System-based modeling prompts expressing the reconstruction performance in terms of *system norms*, thus providing a

unified setup for deterministic and stochastic formulations. In this paper we opt for the L^2 system norm, which corresponds to the mean-square framework that one can find in Wiener/Kalman filtering [19].

The L^2-norm of h-time invariant systems is defined through their lifted frequency responses; see [11, Sec. V-D] and the references therein. For the discussion in this part, however, it is sufficient to elaborate on deterministic and stochastic interpretations of this definition.

For the deterministic interpretation, partition $\mathcal{G}_{\mathrm{e}}$ as

$$\mathcal{G}_{\mathrm{e}} = \begin{bmatrix} \mathcal{G}_{\mathrm{e},v} & \mathcal{G}_{\mathrm{e},n} \end{bmatrix} := \begin{bmatrix} \mathcal{G}_v - \mathcal{H}\bar{\mathcal{F}}\mathcal{S}\mathcal{G}_y & -\mathcal{H}\bar{\mathcal{F}}\Sigma^{1/2} \end{bmatrix}$$

according to the partition of w. Assuming, for simplicity, that both w_v and $\bar{w}_n$ are scalar signals, the L^2-norm of the error system satisfies

$$\|\mathcal{G}_{\mathrm{e}}\|_2^2 = \frac{1}{h}\int_0^h \|\mathcal{G}_{\mathrm{e},v}\delta(\cdot-\sigma)\|_{L^2(\mathbb{R})}^2 \,\mathrm{d}\sigma + \frac{1}{h}\|\mathcal{G}_{\mathrm{e},n}\bar{\delta}\|_{L^2(\mathbb{R})}^2.$$

The first component above, which corresponds to the effect of w_v on e, is the average energy of e, where the average is taken over all $w_v(t) = \delta(t-\sigma)$ in $\sigma \in [0,h)$. The second component, which corresponds to the effect of $\bar{w}_n$ on e, is effectively the energy of the interpolation kernel, $\phi(t)$, scaled by Σ/h (it can thus be thought of as a Tikhonov regularization [6]).

In the stochastic setting, $\|\mathcal{G}_{\mathrm{e}}\|_2^2$ equals the over time averaged sum of variances (power) of all n_e elements of e, provided w_v and $\bar{w}_n$ are standard analog and discrete white processes, respectively.

Concluding this section, we would like to emphasize that we see the signal generator $\mathcal{G}$ and the weight on the measurement noise Σ as our tuning parameters, rather than the most accurate reflection of properties of v, y, and $\bar{n}$. The minimization of $\|\mathcal{G}_{\mathrm{e}}\|_2$ is then merely our design tool. In view of this, it may frequently be preferable to trade precision for the simplicity of the resulting solution. This may be manifested in the choice of a low-order $\mathcal{G}$. The choice of the L^2-norm as the performance measure is then motivated, to some extent, by the transparency of the resulting solution procedure and (relatively) easily traceable properties of the resulting reconstructors.

III. Problem Solution

To formulate the solution of $\mathbf{RP_l}$, bring in a *minimal* state-space realization of $G(s)$:

$$G(s) = \begin{bmatrix} G_v(s) \\ G_y(s) \end{bmatrix} = \begin{bmatrix} C_v \\ C_y \end{bmatrix} (sI - A)^{-1} B. \tag{5}$$

Minimality implies that the pair (A, B) is controllable and $\left(\begin{bmatrix} C_v \\ C_y \end{bmatrix}, A\right)$ is observable [20]. Throughout, we make the following assumptions.

$\boldsymbol{\mathcal{A}_1}$: $\left(C_y, \mathrm{e}^{Ah}\right)$ has no unobservable modes in $\mathbb{C} \setminus \mathbb{D}$.

$\boldsymbol{\mathcal{A}_2}$: $\begin{bmatrix} C_y & \Sigma \end{bmatrix}$ has full row rank.

Assumption $\boldsymbol{\mathcal{A}_1}$ is necessary for the existence of a reconstructor, stabilizing the error system $\mathcal{G}_{\mathrm{e}}$. It always holds for stable $\mathcal{G}$; otherwise, it implies that all unstable modes of $\mathcal{G}_v$ are also present in the measurement channel $\mathcal{S}\mathcal{G}_y$. Assumption $\boldsymbol{\mathcal{A}_2}$ merely rules out redundant measurements and thus entails no loss of generality.

Introduce the following matrix function of a real argument:

$$\Lambda(t) = \begin{bmatrix} \Lambda_{11}(t) & \Lambda_{12}(t) \\ 0 & \Lambda_{22}(t) \end{bmatrix} := \exp\left(\begin{bmatrix} A & BB' \\ 0 & -A' \end{bmatrix} t\right). \tag{6}$$

We skip the argument when $t = h$, so that we write Λ_{ij} instead of $\Lambda_{ij}(h)$. We shall also need the matrix Δ defined via

$$\begin{bmatrix} \Lambda & \Delta \\ 0 & \Lambda \end{bmatrix} := \exp\left(\begin{bmatrix} A & BB' & 0 & 0 \\ 0 & -A' & C_v'C_v & 0 \\ 0 & 0 & A & BB' \\ 0 & 0 & 0 & -A' \end{bmatrix} h\right) \tag{7}$$

with the natural partitioning to four subblocks Δ_{ij}.

Now, define the discrete algebraic Riccati equation (DARE)

$$Y = \Lambda_{11}\left(Y - YC_y'(\Sigma + C_yYC_y')^{-1}C_yY\right)\Lambda_{11}' + \Lambda_{12}\Lambda_{11}'. \tag{8}$$

Its solution Y is said to be stabilizing if $\Sigma + C_yYC_y'$ is nonsingular and

$$\bar{A}_1 := \Lambda_{11}\left(I - YC_y'\left(\Sigma + C_yYC_y'\right)^{-1}C_y\right) \tag{9}$$

is Schur (i.e., has all its eigenvalues in $\mathbb{D}$); see [21] for details. The stabilizing solution, if it exists, is unique and verifies $Y = Y' \geq 0$. In this case, the discrete Lyapunov equation

$$X = \bar{A}_1'X\bar{A}_1 + C_y'\left(\Sigma + C_yYC_y'\right)^{-1}C_y \tag{10}$$

is always solvable by an $X = X' \geq 0$ (because $\bar{A}_1$ is Schur).

The main result of this paper is as follows:

Theorem 3.1: Let the signal generator $\mathcal{G}$ be given by the minimal realization (5) and suppose that assumptions $\boldsymbol{\mathcal{A}_{1,2}}$ hold. Then DARE (8) admits a unique stabilizing solution $Y > 0$ and, given $l \geq 0$, the solution of $\mathbf{RP_l}$ exists, is unique, and is as shown in Fig. 3. Here $\bar{F}_{\mathrm{c}}(z)$ is the causal discrete filter

$$\bar{F}_{\mathrm{c}}(z) = z(zI - \bar{A}_1)^{-1}\Lambda_{11}YB_\phi$$

and $\bar{F}_{\bar{\mathrm{c}},l}(z)$ is the anti-causal discrete FIR filter

$$\bar{F}_{\bar{\mathrm{c}},l}(z) = \sum_{i=0}^{l-1} \bar{A}_{l-1-i}'B_\phi\, z^{l-i} = (I - z^l\bar{A}_l')(z^{-1}I - \bar{A}_1')^{-1}B_\phi$$

in which

$$\bar{A}_k := \bar{A}_1^k \quad \text{and} \quad B_\phi := C_y'\left(\Sigma + C_yYC_y'\right)^{-1} \tag{11}$$

and $\mathcal{H}$ is a D/A converter with the $(n_v \times 2n)$-valued interpolation kernel with support on $[0,h)$,

$$\phi_h(\tau) := \begin{bmatrix} C_v & 0 \end{bmatrix}\Lambda(\tau - h)\begin{bmatrix} I & Y \\ 0 & I \end{bmatrix}\mathbb{1}_{[0,h)}. \tag{12}$$

The optimal performance is then calculated as

$$\mathcal{J}_l := \|\mathcal{G}_{\mathrm{e}}\|_2^2 = \frac{1}{h}\mathrm{tr}\left(\begin{bmatrix} X_l & I - X_lY \end{bmatrix}\Delta\Lambda^{-1}\begin{bmatrix} Y \\ I \end{bmatrix}\right)$$

with $X_l := X - \bar{A}_l'X\bar{A}_l = \sum_{i=0}^{l-1}\bar{A}_i'C_y'(\Sigma + C_yYC_y')^{-1}C_y\bar{A}_i$.

Proof: See Part II [17]. ∎

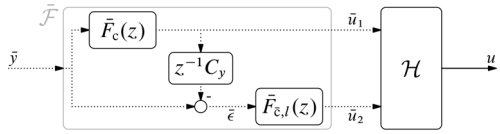

Fig. 3. The optimal l-causal reconstructor $\mathcal{F}_l = \mathcal{H}\bar{\mathcal{F}}$.

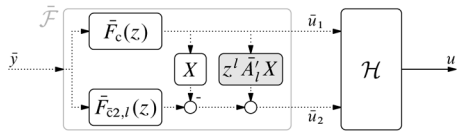

Fig. 4. The optimal l-causal reconstructor with an alternative form of $\bar{\mathcal{F}}$.

In the remainder of this section, we discuss some properties of the optimal solution.

A. Structure and Implementation of $\mathcal{F}_l$

The first component of the digital part $\bar{\mathcal{F}}$ of the reconstructor, $\bar{\mathcal{F}}_{\mathrm{c}}$, is a causal IIR system, which is the Kalman filter for the sampled state vector of $\mathcal{G}$ and can be efficiently implemented as the following state propagation:

$$\bar{u}_1[k] = \bar{A}_1\bar{u}_1[k-1] + \Lambda_{11}YB_\phi\bar{y}[k]. \tag{13}$$

The signal $\bar{\epsilon}$, defined in Fig. 3 as

$$\bar{\epsilon}[k] = \bar{y}[k] - C_y\bar{u}_1[k-1], \tag{14}$$

is then the innovations signal. Finally, $\bar{\mathcal{F}}_{\bar{\mathrm{c}},l}$ is an l-causal FIR system, which can also be implemented via state propagation:

$$\bar{u}_2[k-1] = \bar{A}_1'\bar{u}_2[k] + B_\phi\bar{\epsilon}[k] - \bar{A}_l'B_\phi\bar{\epsilon}[k+l]. \tag{15}$$

Note that this can only be done backward in time, the forward recursion is internally unstable (it contains unstable pole/zero cancellations then).

Remark 3.1 (No Measurement Noise): If $\Sigma = 0$, then (13) and (15) can be simplified by noticing that $\bar{A}_1$ is always singular. Indeed, in this case

$$\bar{A}_1 = \Lambda_{11}\left(I - YC_y'\left(C_yYC_y'\right)^{-1}C_y\right),$$

so that $\bar{A}_1YC_y' = 0$, which means that $\bar{A}_1$ has n_y eigenvalues at the origin. Hence, $(n-n_y)$-order realizations of $\bar{F}_{\mathrm{c}}(z)$ and $\bar{F}_{\bar{\mathrm{c}},l}(z)$ can be constructed, where n is the state dimension.

The digital part of the optimal reconstructor, $\bar{\mathcal{F}}$, admits an alternative form as stated by the following proposition:

Proposition 3.2: Let

$$\bar{F}_{\bar{\mathrm{c}}2,l}(z) = \sum_{i=0}^{l-1}\bar{A}_{l-1-i}'\left(I - \bar{A}_1'X\Lambda_{11}Y\right)B_\phi z^{l-i}.$$

Then, the optimal reconstructor can be equivalently presented in the form depicted in Fig. 4.

Proof: See Appendix A. ∎

The part of this reconstructor without the gray block,

$$\mathcal{F}_{\infty,l} = \mathcal{H}\begin{bmatrix}\bar{\mathcal{F}}_{\mathrm{c}}\\ \bar{\mathcal{F}}_{\bar{\mathrm{c}}2,l} - X\bar{\mathcal{F}}_{\mathrm{c}}\end{bmatrix},$$

is the truncation of the noncausal reconstructor $\mathcal{F}_\infty$ to $\mathbb{Z}_{-l}^+$. The interpolation kernel of $\mathcal{F}_\infty$ can be written as

$$\phi_\infty(t) = \begin{cases}(\phi_{h1}(\tau) - \phi_{h2}(\tau)X)\bar{A}_k\Lambda_{11}YB_\phi & \text{if } k \geq 0\\ \phi_{h2}(\tau)\bar{A}'_{-k-1}(I - \bar{A}_1'X\Lambda_{11}Y)B_\phi & \text{if } k < 0\end{cases} \tag{16}$$

where $k = \lfloor t/h \rfloor$ and $\tau = t - kh$. The truncation of the noncausal solution, however, is not optimal. Its digital part should be complemented by the gray block in Fig. 4, which amounts to adding the interpolation kernel

$$\phi_{\mathrm{corr},l}(t) = \phi_{h2}(\tau)\bar{A}_l'X\bar{A}_{l+k}\Lambda_{11}YB_\phi, \tag{17}$$

to the truncated version of ϕ_∞. We call it the *correction term*. The optimal l-causal interpolation kernel is then given by

$$\phi_l(t) = \begin{cases}\phi_\infty(t) + \phi_{\mathrm{corr},l}(t) & \text{if } t \geq -lh\\ 0 & \text{otherwise.}\end{cases} \tag{18}$$

The correction term is the only part of ϕ_l that depends on the smoothing lag l. If $l \to \infty$, $\phi_{\mathrm{corr},l}$ vanishes (as $\bar{A}_l \to 0$), and we recover the noncausal solution. For a finite l, the correction term affects mainly the part of $\phi_l(t)$ close to $t = -lh$, and its influence diminishes exponentially as t increases.

B. Optimal Performance

The optimal achievable performance level, $\mathcal{J}_l = \|\mathcal{G}_{\mathrm{e}}\|_2^2$, can be presented in two equivalent forms:

$$\mathcal{J}_l = \mathcal{J}_0 - \mathcal{J}_{l,\mathrm{impr}} = \mathcal{J}_\infty + \mathcal{J}_{l,\mathrm{deter}}$$

where $\mathcal{J}_0$ and $\mathcal{J}_\infty$ are the optimal performance levels of $\mathbf{RP_0}$ and $\mathbf{RP_\infty}$, respectively. $\mathcal{J}_0$ is obtained from $\mathcal{J}_l$ of Theorem 3.1 by replacing X_l with 0, while $\mathcal{J}_\infty$ is obtained by replacing X_l with X. In this case,

$$\mathcal{J}_{l,\mathrm{impr}} := \frac{1}{h}\mathrm{tr}\left(\left(X - \bar{A}_l'X\bar{A}_l\right)\begin{bmatrix}I & -Y\end{bmatrix}\Delta\Lambda^{-1}\begin{bmatrix}Y\\ I\end{bmatrix}\right)$$

quantifies the performance improvement with respect to the preview-free case due to the preview of length l and

$$\mathcal{J}_{l,\mathrm{deter}} := \frac{1}{h}\mathrm{tr}\left(\bar{A}_l'X\bar{A}_l\begin{bmatrix}I & -Y\end{bmatrix}\Delta\Lambda^{-1}\begin{bmatrix}Y\\ I\end{bmatrix}\right)$$

quantifies the deterioration with respect to the noncausal case due to imposing the l-causality constraint.

The value of the optimal performance level itself might not be a meaningful quantity. After all, by scaling of the signal generator one can end up with any performance level. What is important is how the smoothing lag l affect $\mathcal{J}_l$. For example, the ratios $\mathcal{J}_l/\mathcal{J}_0$ and $\mathcal{J}_l/\mathcal{J}_\infty$ may be quite useful in justifying the choice of the smoothing lag.

C. Continuity

Continuity, or even a degree of differentiability, may be a desired property of the reconstructed signal in some applications [22]. In this subsection, we study continuity properties of the reconstructed signal u and how these properties are affected by the interpolation constraints.

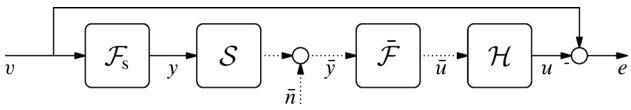

Fig. 5. Sampling and reconstruction analysis setup.

Because $\phi_h(\tau)$ is a smooth function in $(0, h)$, the continuity of $\phi_l(t)$ and, therefore, of $u(t)$ can fail only at the knots $t = kh$. Thus, continuity is equivalent to the condition that

$$\bar{u}_\delta[k] := u(kh + 0) - u(kh - 0) = 0, \quad \forall k \in \mathbb{Z}.$$

The following technical result shows that the sequence $\bar{u}_\delta[k]$ is proportional to the predicted innovations signal $\bar{\epsilon}$ defined in Fig. 3 [see also (14)].

Lemma 3.3: Let $l \in \mathbb{Z}_0^+$, then

$$\bar{u}_\delta[k] = C_v Y \bar{A}_l' B_\phi \, \bar{\epsilon}[k + l]$$

for all $k \in \mathbb{Z}$.

Proof: See Appendix A. ∎

As the transfer function $I - z^{-1} C_y \bar{F}_c(z)$ from $\bar{\epsilon}$ to $\bar{y}$ is invertible, the continuity of $u(t)$ for every $\bar{y}$ is equivalent to the condition [mind (11)]

$$C_v Y \bar{A}_l' C_y' = 0. \tag{19}$$

Because $\bar{A}_l$ vanishes as $l \to \infty$, we can conclude that the noncausal solution is always continuous. Imposing causality constraints, however, might destroy continuity. Although condition (19) is easy to check numerically, it is not quite useful in giving us a generic insight into the class of reconstruction problems for which the l-causal solution is continuous.

In a particular case when $\mathcal{G}_v = \mathcal{G}_y$ a more transparent sufficient condition can be derived from (19). Namely, by (9), we have $C_y Y A_1' = \Sigma(\Sigma + C_y Y C_y')^{-1} C_y Y \Lambda_{11}'$, so that the continuity condition (19) for $l \geq 1$ reads

$$\Sigma \left(\Sigma + C_y Y C_y'\right)^{-1} C_y Y \Lambda_{11}' \bar{A}_{l-1}' C_y' = 0$$

and holds whenever $\Sigma = 0$. In other words, when $y = v$, the relaxedly causal reconstruction is continuous if no measurement noise is assumed. This might appear counterintuitive as the addition of the measurement noise is expected to render the reconstruction more cautious. In any case, the reconstruction with no preview ($l = 0$) is always discontinuous because $C_y Y C_y' > 0$, which violates (19) for $l = 0$.

IV. Frequency-Domain Analysis

The design setup in Fig. 2 involves weighting parameters $\mathcal{G}$ and Σ, which normally contain fictitious components used to shape properties of the optimal solution. Once the reconstructor is designed, however, it might be of interest to analyze its properties with respect to "real" signals, which are v and, possibly, $\bar{n}$. In this section we consider frequency-domain properties of the reconstruction setup in Fig. 5, where $\mathcal{S}$ is the ideal sampler and $\mathcal{F}_s$ is an analog filter, representing the sensing mechanism, so that the cascade $\mathcal{S}\mathcal{F}_s$ may be viewed as a nonideal acquisition devise. To simplify the exposition, we also assume that v and $\bar{n}$ are scalar signals. MIMO extensions are straightforward.

A. Frequency Power Response

One of the reasons that the frequency response is such a popular tool is that it allows to graphically present the frequency-dependent behavior of a system, provided that the system is time invariant. Extensions to h-shift invariant systems, like that in Fig. 5, are not that straightforward. For instance, applying the harmonic $v(t) = \mathrm{e}^{\mathrm{j}\omega t}$, we end up with

$$\begin{aligned} u(kh + \tau) &= \sum_{i \in \mathbb{Z}} \phi_l(ih + \tau) \bar{y}[k - i] \\ &= \sum_{i \in \mathbb{Z}} \phi_l(ih + \tau) \mathrm{e}^{\mathrm{j}\omega(k-i)h} F_s(\mathrm{j}\omega) \\ &= \mathrm{e}^{\mathrm{j}\omega kh} \sum_{i \in \mathbb{Z}} \phi_l(ih + \tau) \mathrm{e}^{-\mathrm{j}\omega ih} F_s(\mathrm{j}\omega) \\ &= \mathrm{e}^{\mathrm{j}\omega kh} \frac{1}{h} \sum_{i \in \mathbb{Z}} \Phi_l(\mathrm{j}\omega_i) \mathrm{e}^{\mathrm{j}\omega_i \tau} F_s(\mathrm{j}\omega) \end{aligned}$$

where $\Phi_l(\mathrm{j}\omega)$ is the Fourier transform of the interpolation kernel $\phi_l(t)$, $\omega_i := \omega + 2\omega_N i$ are the aliases of ω, and the last equality follows by [11, eq. (17b)]. Because $\mathrm{e}^{\mathrm{j}\omega kh} = \mathrm{e}^{\mathrm{j}\omega_i kh}$ for all $i \in \mathbb{Z}$, we have that

$$u(t) = \frac{1}{h} \sum_{i \in \mathbb{Z}} \Phi_l(\mathrm{j}\omega_i) \mathrm{e}^{\mathrm{j}\omega_i t} F_s(\mathrm{j}\omega). \tag{20}$$

In contrast to shift invariant systems, it is hard to relate this output $u(t)$ to its harmonic input $v(t) = \mathrm{e}^{\mathrm{j}\omega t}$.

There are generalization of the notion of the frequency response to sampled-data (and other periodic) systems; see [23] and the references therein. To account for possible folding effects, these generalizations determine the frequency response at each frequency as an infinite-dimensional operator, which, again, is hard to visualize. The magnitude frequency response, defined then as a norm of such operators, has all aliased frequencies ω_k mixed up in it. This is fine for the analysis of system norms, but less appropriate for a harmonic analysis. In fact, if applied to the system from v to e in Fig. 5, the methods presented in [23] would result in the frequency response gain larger than one at each frequency, which makes no sense.

In this paper we adopt an alternative approach to visualize frequency-domain properties of sampled-data system. Given a linear system $\mathcal{G}$, define its frequency power response (FPR) as

$$\mathrm{FPR}_{\mathcal{G}}(\omega) := \lim_{T \to \infty} \frac{1}{2T} \int_{-T}^{T} |(\mathcal{G}\mathrm{e}^{\mathrm{j}\omega t})(t)|^2 \, \mathrm{d}t.$$

It is the power of the output when driven by a unit-power harmonic input of frequency ω. This function is well defined for all $\omega \in \mathbb{R}$, provided $\mathcal{G}$ is h-shift invariant and L^2-stable, and allows us to visualize the behavior of the system, very similar to what the magnitude frequency response does for shift-invariant systems. In fact, if $\mathcal{G}$ is shift invariant, then $\mathrm{FPR}_{\mathcal{G}}(\omega) = |G(\mathrm{j}\omega)|^2$. For linear h-shift invariant systems, we have that

$$\begin{aligned} |(\mathcal{G}\mathrm{e}^{\mathrm{j}\omega t})(t + h)| &= |(\mathcal{G}\mathrm{e}^{\mathrm{j}\omega(t+h)})(t)| = |(\mathcal{G}\mathrm{e}^{\mathrm{j}\omega t})(t) \, \mathrm{e}^{\mathrm{j}\omega h}| \\ &= |(\mathcal{G}\mathrm{e}^{\mathrm{j}\omega t})(t)| \end{aligned}$$

where the first equality follows by h-shift invariance and the second one by linearity. Therefore, if $\mathcal{G}$ is h-shift invariant its FPR can be determined by an average energy over one period

$$\mathrm{FPR}_{\mathcal{G}}(\omega) = \frac{1}{h}\int_0^h |(\mathcal{G}\mathrm{e}^{\mathrm{j}\omega t})(t)|^2\,\mathrm{d}t. \tag{21}$$

Consider now the FPR of the system from v to e in Fig. 5. With some abuse of notation, we denote it $\mathrm{FPR}_{ev}(\omega)$. Combining (21) and (20), we have

$$\begin{aligned}\mathrm{FPR}_{ev}(\omega) &= \frac{1}{h}\int_0^h \left|\mathrm{e}^{\mathrm{j}\omega t} - \frac{1}{h}\sum_{i\in\mathbb{Z}} \Phi_l(\mathrm{j}\omega_i)\mathrm{e}^{\mathrm{j}\omega_i t}F_{\mathrm{s}}(\mathrm{j}\omega)\right|^2 \mathrm{d}t \\ &= \frac{1}{h}\int_0^h \left|1 - \frac{1}{h}\sum_{i\in\mathbb{Z}} \Phi_l(\mathrm{j}\omega_i)\mathrm{e}^{\mathrm{j}2\pi i t/h}F_{\mathrm{s}}(\mathrm{j}\omega)\right|^2 \mathrm{d}t \\ &= 1 - \frac{2}{h}\mathrm{Re}\{\Phi_l(\mathrm{j}\omega)F_{\mathrm{s}}(\mathrm{j}\omega)\} \\ &\quad + \frac{1}{h^2}\sum_{i\in\mathbb{Z}} |\Phi_l(\mathrm{j}\omega_i)|^2|F_{\mathrm{s}}(\mathrm{j}\omega)|^2 \end{aligned}\tag{22}$$

where the last equality is due to the fact that all harmonic functions $\mathrm{e}^{\mathrm{j}2\pi i t/h}$ for $i \neq 0$ integrate to zero (cf. the proof of [11, Prop. 5.1]). We thus just proved the following result.

Theorem 4.1: Let the system from v to e in Fig. 5 be L^2 stable. Then, its frequency power response is

$$\begin{aligned}\mathrm{FPR}_{ev}(\omega) = \left|1 - \frac{1}{h}\Phi_l(\mathrm{j}\omega)F_{\mathrm{s}}(\mathrm{j}\omega)\right|^2 \\ + \frac{1}{h^2}\sum_{i\in\mathbb{Z}\setminus\{0\}} |\Phi_l(\mathrm{j}\omega_i)|^2|F_{\mathrm{s}}(\mathrm{j}\omega)|^2.\end{aligned}\tag{23}$$

Proof: The right-hand side of (23) equals (22). ∎

Remark 4.1: The two terms of the right-hand side of (23) have neat interpretations. The first term would be the FPR (in fact, the squared magnitude frequency response) of the error system if v were reconstructed directly from the analog measurement y by an analog LTI filter having the impulse response $\phi_l(t)$, i.e., if no sampling were present. The second term characterizes the deterioration of the reconstruction performance due to the sampling process. This amounts to the powers of all aliased components of the interpolation kernel weighted by $|F_{\mathrm{s}}(\mathrm{j}\omega)|^2$, which is intuitive. ▽

Remark 4.2: Formula (23) is known in the literature as the *error kernel* [2]. As shown in [24, Theorem 2],

$$\frac{1}{h}\int_0^h \|e_\tau\|_2^2\,\mathrm{d}\tau = \frac{1}{2\pi}\int_{-\infty}^{\infty} \mathrm{FPR}_{ev}(\omega)|v(\mathrm{j}\omega)|^2\,\mathrm{d}\omega$$

where $e_\tau(t)$ is the error of reconstructing $v(t-\tau)$ and $\|\cdot\|_2$ stands for the $L^2(\mathbb{R})$ signal norm. If $v(\mathrm{j}\omega) = G_v(\mathrm{j}\omega)$, then the relation above is the square of the L^2 norm of the system from w, which is the input of $\mathcal{G}_v$, to e [11, Sec. V-D], which is exactly what we minimize in the noise-free case. Thus,

$$\mathcal{J}_l = \|\mathcal{G}_{\mathrm{e}}\|_2^2 = \frac{1}{2\pi}\int_{-\infty}^{\infty} \mathrm{FPR}_{ev}(\omega)|G_v(\mathrm{j}\omega)|^2\,\mathrm{d}\omega \tag{24}$$

whenever $\Sigma = 0$. ∎

Hitherto we only considered the effect of the analog signal v on the reconstruction error e. We may also be interested in the sensitivity of this error to the discrete measurement noise $\bar{n}$. For an D/A system $\mathcal{G}$, like that from $\bar{n}$ to e in Fig. 5, the counterpart of the FPR is

$$\mathrm{FPR}_{\mathcal{G}}(\theta) = \frac{1}{h}\int_0^h |(\mathcal{G}\mathrm{e}^{\mathrm{j}\theta k})(t)|^2\,\mathrm{d}t, \quad \theta \in [-\pi, \pi].$$

By repeating our previous arguments replacing $\omega \to \theta/h$, we end up with

$$\mathrm{FPR}_{e\bar{n}}(\theta) = \frac{1}{h^2}\sum_{i\in\mathbb{Z}} |\Phi_l(\mathrm{j}\theta_i/h)|^2 \tag{25}$$

where $\theta_i := \theta + 2\pi i$. This function can be used to analyze noise sensitivity of our reconstruction.

B. Computational Issues

To evaluate the FPRs in (23) and (25), we need to compute the Fourier transform of the interpolation kernel ϕ_l and the folding of its squared magnitudes. Below we discuss how these computations can be efficiently performed in terms of the state-space realization (5).

We start with the optimal $\Phi_l(\mathrm{j}\omega)$. It follows from the form of the optimal reconstructor in Fig. 3 that

$$\Phi_l(\mathrm{j}\omega) = \Phi_h(\mathrm{j}\omega)\bar{F}(\mathrm{e}^{\mathrm{j}\omega h})$$

where

$$\Phi_h(\mathrm{j}\omega) = \begin{bmatrix} C_v & 0\end{bmatrix}\int_0^h \Lambda(\tau - h)\mathrm{e}^{-\mathrm{j}\omega\tau}\,\mathrm{d}\tau \begin{bmatrix} I & Y \\ 0 & I\end{bmatrix}$$

is the Fourier transform of the hold function ϕ_h in (12) and $\bar{F}(\mathrm{e}^{\mathrm{j}\omega h})$ is the frequency response of the discrete part of the reconstructor, $\bar{\mathcal{F}}$. If $\mathrm{j}\omega$ is not an eigenvalue of A, then it follows from (6) that

$$\begin{aligned}\Phi_h(\mathrm{j}\omega) = C_v\begin{bmatrix}\Lambda'_{22} - \mathrm{e}^{-\mathrm{j}\omega h}I & -\Lambda'_{12}\end{bmatrix} \\ \times \begin{bmatrix}\mathrm{j}\omega I - A & -BB' \\ 0 & \mathrm{j}\omega I + A'\end{bmatrix}^{-1}\begin{bmatrix} I & Y \\ 0 & I\end{bmatrix}\end{aligned}$$

where the formula (30) from the Appendix A was used. If $\mathrm{j}\omega$ is an eigenvalue of A, the function above has a removable singularity at this point, rendering this formula not well suitable for calculations. In this case, an alternative expression can be obtained using Lemma A.1 in the Appendix A (with $F = 0$):

$$\begin{aligned}\Phi_h(\mathrm{j}\omega) = \mathrm{e}^{-\mathrm{j}\omega h}\begin{bmatrix} C_v & 0 & 0 & 0\end{bmatrix} \\ \times \exp\left(\begin{bmatrix}\mathrm{j}\omega I - A & -BB' & I & Y \\ 0 & \mathrm{j}\omega I + A' & 0 & I \\ 0 & 0 & 0 & 0 \\ 0 & 0 & 0 & 0\end{bmatrix} h\right)\begin{bmatrix} 0 & 0 \\ 0 & 0 \\ I & 0 \\ 0 & I\end{bmatrix}.\end{aligned}$$

This formula requires the computation of a matrix exponential at each frequency, which is computationally quite involved. Hence, this formula should be used only around pure imaginary eigenvalues of A.

Remark 4.3: Combining $\Phi_h(\mathrm{j}\omega)$ with $\bar{F}(\mathrm{e}^{\mathrm{j}\omega h})$ and exploiting the state-space structure of the latter, an alternative expression

for $\Phi_l(\mathrm{j}\omega)$ can be derived. To this end, introduce the discrete transfer function

$$\begin{aligned}\bar{\chi}(z) &:= \left(I - z\bar{F}_{\mathrm{c}}'(z^{-1})C_y'\right)\left(\Sigma + C_y Y C_y'\right)\left(I - z^{-1}C_y\bar{F}_{\mathrm{c}}(z)\right)\\ &= \left(\Sigma - z\begin{bmatrix}C_y & 0\end{bmatrix}(zI-\Lambda)^{-1}\begin{bmatrix}0\\ C_y'\end{bmatrix}\right)^{-1}\\ &= \left(\Sigma + \frac{1}{h}\sum_{k\in\mathbb{Z}} G_y(s_k)G_y'(-s_k)\right)^{-1}\end{aligned}$$

where $s_k := \frac{1}{h}\mathrm{Ln}z + \mathrm{j}2\omega_{\mathrm{N}}k$ and $\mathrm{Ln}z$ stands for the principal value of $\ln z$. It can be shown, by some tedious albeit quite straightforward algebra, that

$$\Phi_l(\mathrm{j}\omega) = \Phi_\infty(\mathrm{j}\omega) + \Phi_{\mathrm{a},l}(\mathrm{j}\omega)$$

where

$$\Phi_\infty(\mathrm{j}\omega) = G_v(\mathrm{j}\omega)G_y'(-\mathrm{j}\omega)\bar{\chi}(\mathrm{e}^{\mathrm{j}\omega h})$$

is the frequency response of the noncausal reconstructor given by (16) (cf. [5, eq. (10)]) and

$$\Phi_{\mathrm{a},l}(\mathrm{j}\omega) = C_v\Phi_{h2}(\mathrm{j}\omega)\mathrm{e}^{\mathrm{j}\omega hl}\bar{A}_l'(I - \mathrm{e}^{\mathrm{j}\omega h}\Lambda_{11}')^{-1}C_y'\bar{\chi}(\mathrm{e}^{\mathrm{j}\omega h})$$

is the Fourier transform of the term, comprised of the truncation of ϕ_∞ to $(-\infty, lh)$ and $\phi_{\mathrm{corr},l}$ defined by (17). Note that $\Phi_{\mathrm{a},l}$ vanishes as $l \to \infty$. ∎

The infinite sums in the FPR formulas (23) and (25) shall not be computed directly. Instead, note that the interpolation kernel $\phi_h(t)$ has support in $[0, h)$. Hence, its lifted transfer function is static and the application of [11, Prop. 5.2] yields

$$\sum_{i\in\mathbb{Z}} |\Phi_l(\mathrm{j}\omega_i)|^2 = h^2\bar{F}'(\mathrm{e}^{-\mathrm{j}\omega h})M_h\bar{F}(\mathrm{e}^{\mathrm{j}\omega h})$$

where

$$M_h := \frac{1}{h}\int_0^h \phi_h'(\tau)\phi_h(\tau)\,\mathrm{d}\tau$$

is a $2n \times 2n$ matrix [cf. (12)]. To compute M_h we can again make use of Lemma A.1. Exploiting then the fact that

$$-\begin{bmatrix}A & BB'\\ 0 & -A'\end{bmatrix}' = \begin{bmatrix}0 & I\\ -I & 0\end{bmatrix}\begin{bmatrix}A & BB'\\ 0 & -A'\end{bmatrix}\begin{bmatrix}0 & -I\\ I & 0\end{bmatrix}$$

we end up with [the matrix Δ below is defined by (7)]

$$M_h = \frac{1}{h}\begin{bmatrix}0 & I\\ -I & Y\end{bmatrix}\Delta\Lambda^{-1}\begin{bmatrix}I & Y\\ 0 & I\end{bmatrix} \tag{26}$$

which is readily calculable.

V. Causal Cardinal Cubic B-Splines

To illustrate the proposed approach we consider in this section the $\mathbf{RP_l}$ for

$$G_v(s) = G_y(s) = \frac{1}{s^2} \quad \text{and} \quad \Sigma = 0.$$

This choice of the signal generator can be thought of as reflecting a low-pass dominance of the signal to be reconstructed and the requirement to have the zero steady-state error for step and ramp components of v. In the noncausal case this $\mathcal{G}$ results (see [5, Theorem 3.3]) in the cardinal cubic B-splines of [7], which are perhaps the most extensively studied polynomial splines. This renders this case suitable for comparing the proposed approach to the design of l-causal reconstructors with conventional l-causal reconstructors obtained by ad hoc truncations of noncausal interpolation kernels.

A. Solution

Bring in any minimal state-space realization of $\mathcal{G}$, say

$$G(s) = \left[\begin{array}{cc}1 & 0\\ \hline 1 & 0\end{array}\right]\left(sI - \begin{bmatrix}0 & 1/h\\ 0 & 0\end{bmatrix}\right)^{-1}\begin{bmatrix}0\\ h\end{bmatrix}. \tag{27}$$

Obviously, $\boldsymbol{\mathcal{A}_2}$ holds. As $\mathrm{e}^{Ah} = \begin{bmatrix}1 & 1\\ 0 & 1\end{bmatrix}$, the observability matrix of (C_y, e^{Ah}) is $\begin{bmatrix}1 & 0\\ 1 & 1\end{bmatrix}$, which is nonsingular. Hence, $\boldsymbol{\mathcal{A}_1}$ holds as well, and the problem is solvable.

Denoting

$$\alpha := \sqrt{3} - 2 \approx -0.2679, \tag{28}$$

the formulas of Theorem 3.1 and Proposition 3.2 yield the discrete filters

$$\bar{F}_{\mathrm{c}}(z) = \begin{bmatrix}4-\sqrt{3}\\ 3-\sqrt{3}\end{bmatrix} + \begin{bmatrix}1\\ 1\end{bmatrix}\frac{6\alpha}{z-\alpha},$$

$$\bar{F}_{\tilde{\mathrm{c}}2,l}(z) = \frac{6\,z}{h^3}\left(\begin{bmatrix}3\sqrt{3}-3\\ -\sqrt{3}\end{bmatrix}\sum_{i=1}^{l-1}(\alpha z)^{l-i} + \begin{bmatrix}4-3\sqrt{3}\\ 1-\sqrt{3}\end{bmatrix}\right),$$

the Lyapunov solution

$$X = \frac{1}{h^3}\begin{bmatrix}6\sqrt{3}-6 & 3-3\sqrt{3}\\ 3-\sqrt{3} & \sqrt{3}\end{bmatrix},$$

the "correction" gain (if $l \geq 1$)

$$\bar{A}_l'X = \frac{\alpha^l}{h^3}\begin{bmatrix}6\sqrt{3} & 3-3\sqrt{3}\\ -3-3\sqrt{3} & \sqrt{3}\end{bmatrix},$$

and the two components of the interpolation kernels of $\mathcal{H}$

$$\phi_{h1}(\tilde{\tau}) = \begin{bmatrix}1 & \tilde{\tau}-1\end{bmatrix}\mathbb{1}_{[0,h]},$$

$$\phi_{h2}(\tilde{\tau}) = \frac{h^3\tilde{\tau}}{6}\begin{bmatrix}-\tilde{\tau}^2 + 3\tilde{\tau} + \sqrt{3} & 3\tilde{\tau} + \sqrt{3}\end{bmatrix}\mathbb{1}_{[0,h]}$$

where $\tilde{\tau} := \tau/h$ is the normalized intersample time. Note that $\bar{F}_{\mathrm{c}}(z)$ is a first-order transfer function, which agrees with the discussion in Remark 3.1.

Now, combining discrete filters with corresponding holds, we end up with the optimal interpolation kernel of the form (18) with

$$\phi_\infty((k+\tilde{\tau})h) = \begin{cases}\tilde{\phi}_1(1-\tilde{\tau})\,\alpha^{-k-1} & \text{if } k \leq -2\\ \tilde{\phi}_0(1-\tilde{\tau}) & \text{if } k = -1\\ \tilde{\phi}_0(\tilde{\tau}) & \text{if } k = 0\\ \tilde{\phi}_1(\tilde{\tau})\,\alpha^{k} & \text{if } k \geq 1\end{cases}$$

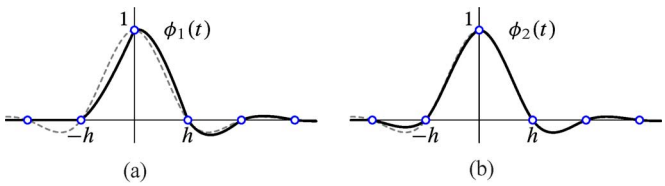

Fig. 6. Interpolation kernels $\phi_l(t)$ of l-causal cardinal cubic splines. (a) Smoothing lag $l = 1$, (b) Smoothing lag $l = 2$.

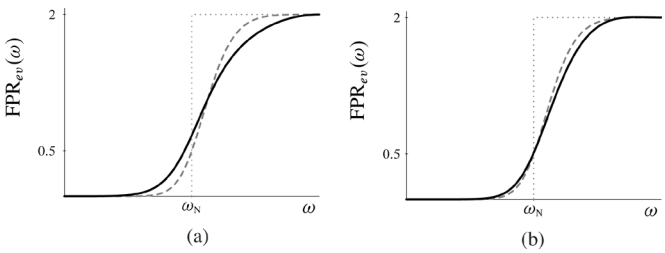

Fig. 7. FPRs with $G_v(s) = 1/s^2$ and $F_s(s) = 1$. (a) Smoothing lag $l = 1$. (b) Smoothing lag $l = 2$.

and

$$\phi_{\mathrm{corr},l}((k+\tilde{\tau})h) = \begin{cases} -\tilde{\phi}_1(1-\tilde{\tau})\frac{3-\sqrt{3}}{3}\alpha^{l-1} & \text{if } k = -l \\ -\tilde{\phi}_1(1-\tilde{\tau})\alpha^{2l+k-1} & \text{if } k \geq 1-l \end{cases}$$

where

$$\tilde{\phi}_0(\tilde{\tau}) := (1-\tilde{\tau})(1+\tilde{\tau}-(3\sqrt{3}-4)\tilde{\tau}^2)$$
$$\tilde{\phi}_1(\tilde{\tau}) := 3\tilde{\tau}(1-\tilde{\tau})(1-(\sqrt{3}-1)\tilde{\tau}).$$

The resulting $\phi_l(t)$ for $l = 1$ and $l = 2$ are shown by the solid lines in Fig. 6 (the gray dashed lines there correspond to the noncausal solution $\phi_\infty(t)$). As l increases, the correction term $\phi_{\mathrm{corr},l}(t)$, which is the difference between the solid and dashed lines in Fig. 6, vanishes, so $\phi_3(t)$ is then barely distinguishable from the truncation of the noncausal solution $\phi_\infty(t)$. For small l, however, $\phi_{l,\mathrm{corr}}$ has a substantial effect on ϕ_l.

The optimal performance

$$\mathcal{J}_l = \frac{10\sqrt{3}-3+11(3+2\sqrt{3})\alpha^{2l}}{2520}h^3$$

is proportional to h^3. As l increases, $\mathcal{J}_l$ decreases exponentially to $\mathcal{J}_\infty$. The following table gives some indications about the decay rate:

l	0	1	2	3
$\mathcal{J}_l/\mathcal{J}_\infty - 1$	4.9653	0.3565	0.0256	0.0018

As we can see, one step preview makes a big difference with respect to the causal reconstruction: it reduces the achievable performance level from $\approx$ 500% of $\mathcal{J}_\infty$ to $\approx$ 36% of it. With three steps preview, we are already within 2‰ of $\mathcal{J}_\infty$.

The frequency power responses $\mathrm{FPR}_{ev}(\omega)$ of the reconstruction for $l = 1, 2$ are presented in Fig. 7. The plots are calculated by (23) and the dashed lines present the noncausal case, $l = \infty$. We are mostly interested in the frequency range $\omega < \omega_\mathrm{N}$ as the performance deteriorates rapidly above the Nyquist frequency. It can be seen that within this range[2] the error power is a monotonically increasing function of ω. This is the result of our choice of the weighting function, $G_v(s) = 1/s^2$, which places more emphasis on low frequencies; cf. (24). The presence of a double pole at the origin in $G_v(s)$ effectively imposes the interpolation constraints $\mathrm{FPR}_{ev}(0) = \dot{\mathrm{FPR}}_{ev}(0) = 0$. For $l = 1$ and $l = 2$, the noncausal reconstruction outperforms its causal counterparts at every $\omega \leq \omega_\mathrm{N}$. This is no longer true for $l \geq 3$, where there are frequency ranges within $[0, \omega_\mathrm{N}]$ where causal reconstructors yield slightly (up to about $3.3 \cdot 10^{-4}$) better performance.

B. Comparisons With the Results of [9]

We have already argued that the reconstructors obtained in the previous subsection may be regarded as causal cardinal cubic splines. It is then of interest to compare these splines with those available in the literature. A convenient starting point for this is the recent work [9], where several ad hoc truncation approaches are studied and their performance is compared by numerical simulations. For the comparison purpose we pick the so-called C-cascade splines, say $\phi_{\mathrm{C-cas}}$, which produced the best results over all other causal splines considered in [9], and compare them with ϕ_l by their closeness to the noncausal cubic splines, ϕ_∞.

First, following [9], consider the problem of reconstructing the bandlimited triangle wave [see Fig. 8(a)]

$$v(t) = \sum_{i=1}^{4} \frac{8(-1)^{i-1}}{(2i-1)^2\pi^2} \sin\left(\frac{2\pi(2i-1)}{16h}\,t\right) \qquad (29)$$

from its samples $\bar{y}[k] = v(kh)$ [big dots in Fig. 8(a); small filled dots will be explained in Section V-D]. Fig. 8(b)–(d) presents steady-state (stationary) reconstruction errors $e(t)$ over one period of $16h$ for three different smoothing lags $l = 1, 2, 3$, together with the noncausal case (dashed gray lines).[3] One can see that the error in noncausal reconstruction is symmetric around the points $4h$ and $12h$, which are the points where $v(t)$ abruptly changes its direction (in between, v is close to the ramp, for which the reconstructions are optimal). The symmetry is not maintained in causal solutions. This is especially visible in the case of $l = 1$, where the preview available to the reconstructor is too short to anticipate this direction change. The deviation from the reconstruction with the noncausal splines may be quantified by the power $P_{u_\infty - u_l} := \lim_{T\to\infty} \frac{1}{T}\int_{-T/2}^{T/2}(u_\infty(t)-u_l(t))^2\,\mathrm{d}t$ of the difference between $u_\infty(t)$ and $u_l(t)$, which are the signals reconstructed by the noncausal and l-causal splines, respectively. Remarkably, each additional preview step reduces this quantity by the very same factor of $1/\alpha^2 = 7 + 4\sqrt{3} \approx 13.93$.

The case of $l = 3$ [Fig. 8(d)] corresponds to the setup studied by Petrinović, so we may compare our reconstructor (causal spline) with those proposed in [9]. It is readily seen from Fig. 8(d) that our reconstruction virtually coincides with that obtained by the noncausal spline in every interval but in

[2]This is not true at higher frequencies, in fact, $\mathrm{FPR}_{ev}(\omega)$ for every l has local minima at all $\omega = (2k+1)\omega_\mathrm{N}$, $k \in \mathbb{N}$.

[3]The plots in Fig. 8(b) and (c) are clipped above 0.01. The clipped parts can be easily recovered because the second halves of these curves are merely the glide reflections of their first halves.

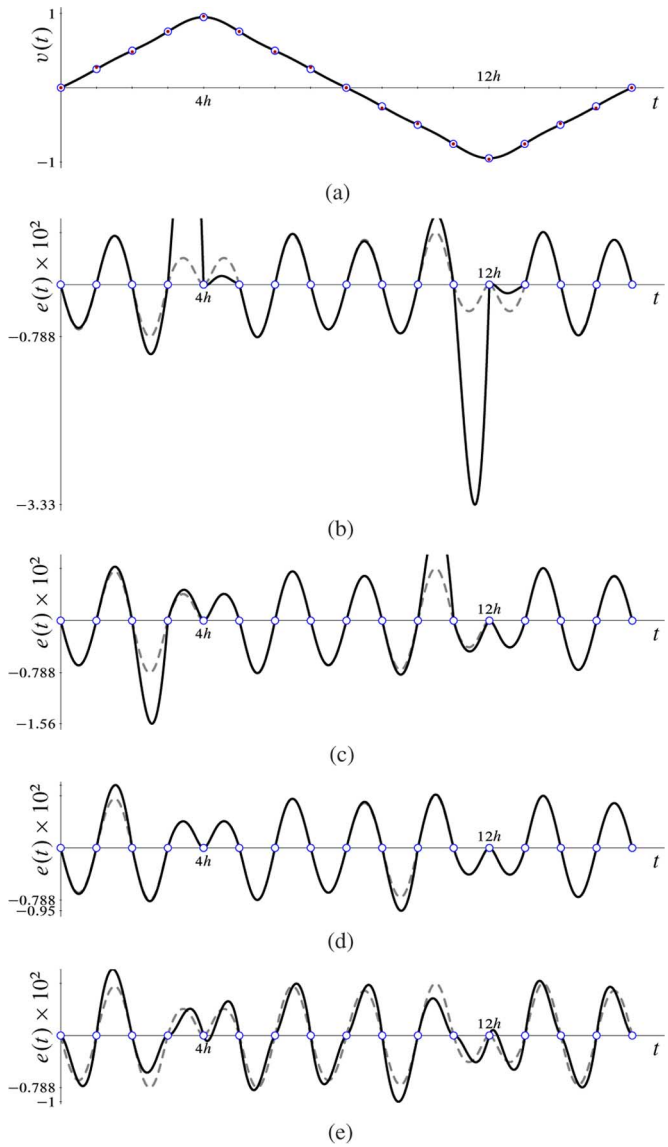

Fig. 8. Reconstructing the bandlimited triangle wave (29). (a) Signal to be reconstructed, (29), (b) Reconstruction error for $l = 1$ ($P_{u_\infty - u_1} = 5.5428 \times 10^{-5}$), (c) Reconstruction error for $l = 2$ ($P_{u_\infty - u_2} = 3.9795 \times 10^{-6}$), (d) Reconstruction error for $l = 3$ ($P_{u_\infty - u_3} = 2.8572 \times 10^{-7}$), (e) Reconstruction error for $l = 3$ and the C-cascade splines of [9] ($P_{u_\infty - u_{\mathrm{C-cas}}} = 2.1322 \times 10^{-6}$).

$(h, 2h)$ and $(9h, 10h)$. Reconstruction errors with the causal splines proposed by Petrinović are visibly different from the noncausal case in every interval; see Fig. 8(e). This impression is confirmed quantitatively: $P_{u_\infty - u_{\mathrm{C-cas}}}$ is larger than $P_{u_\infty - u_3}$ almost by a factor of 7.5. The peak value of the analog error in our case, 0.01, is also more than 5% smaller than that attainable by the causal C-cascade splines.

Another option for comparing the closeness of causal cubic splines to their noncausal versions is via the power of the deviation from the noncausal reconstruction of a single harmonic $v(t) = \mathrm{e}^{\mathrm{j}\omega t}$. These quantities can be calculated by arguments similar to those presented in Section IV. Fig. 9 presents the ratio between such powers for our reconstructor and for the causal C-cascade cubic splines as a function of the frequency ω. This plot shows that ϕ_3 is, in a sense, a better approximation of ϕ_∞

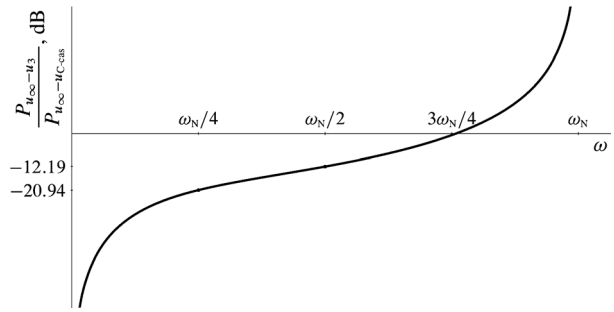

Fig. 9. Comparison with C-cascade cubic splines of [9] for $l = 3$.

up to about three quarters of the Nyquist frequency ω_{N}, after which the causal C-cascade splines become a more accurate imitation of ϕ_∞. In the frequency range $(3\omega_{\mathrm{N}}/4, \omega_{\mathrm{N}})$, however, the reconstruction is rather inaccurate. The peak value of the reconstruction error there is at least 25% of the input magnitude. This might question the suitability of the cubic splines for reconstructing such rapid signals.

C. Reconstructing $\dot{v}(t)$

Our approach seamlessly extends to the case when $v \neq y$. To demonstrate this, consider the problem of reconstructing the derivative of y from the sampled measurements of y under the same assumptions as those used in the beginning of this section. This problem, corresponds to the choice of $G_v(s) = \frac{1}{s}$ and $G_y(s) = \frac{1}{s^2}$ or to the following state-space realization of $\mathcal{G}$:

$$G(s) = \left[\begin{array}{cc} 0 & 1/h \\ 1 & 0 \end{array}\right] \left(sI - \left[\begin{array}{cc} 0 & 1/h \\ 0 & 0 \end{array}\right] \right)^{-1} \left[\begin{array}{c} 0 \\ h \end{array}\right].$$

The only difference from (27) is the C_v parameter. This, in turn, implies that only ϕ_h changes comparing with the formulas of Section V-A (the other components do not depend on C_v). We then have

$$\phi_h(\tilde{\tau}) = \frac{h^2}{6} \left[0 \quad 6/h^3 \quad -3\tilde{\tau}^2 + 6\tilde{\tau} + \sqrt{3} \quad 6\tilde{\tau} + \sqrt{3} \right] \mathbb{1}_{[0,h]},$$

with $\tilde{\tau} := \tau/h$, as before.

The impulse response of the optimal reconstructor is again of the form $\phi_l(t) = \phi_\infty(t) + \phi_{\mathrm{corr},l}(t)$, for the same ϕ_∞ and $\phi_{\mathrm{corr},l}$ as in the previous example, modulo the substitutions

$$\tilde{\phi}_0(\tilde{\tau}) \to \frac{\mathrm{d}}{\mathrm{d}\tau}\tilde{\phi}_0(\tilde{\tau}) = \frac{3}{h}\tilde{\tau}(2 - 2\sqrt{3} + (3\sqrt{3} - 4)\tilde{\tau})$$
$$\tilde{\phi}_1(\tilde{\tau}) \to \frac{\mathrm{d}}{\mathrm{d}\tau}\tilde{\phi}_1(\tilde{\tau}) = \frac{3}{h}(1 - 2\sqrt{3}\tilde{\tau} + 3(\sqrt{3} - 1)\tilde{\tau}^2)$$

(and then $\tilde{\phi}_i(1 - \tilde{\tau}) \to -\frac{\mathrm{d}}{\mathrm{d}\tau}\tilde{\phi}_i(1 - \tilde{\tau})$, $i = 0, 1$), so that this ϕ_l is the derivative of the impulse response of the causal cubic splines in the previous example. This, actually, implies that the optimal reconstruction in this case is *consistent*. Indeed, integrating and then sampling this impulse response (this is exactly our measurement system) will produce the Kronecker delta. The impulse response plots for the cases of $l = 1$ and $l = 2$ are presented in Fig. 10. These impulse responses are no longer continuous functions of t, although the noncausal solution (gray dashed lines) is. This was expectable, taking into account the nondifferentiability of the causal cubic splines in Fig. 6 at the sampling points.

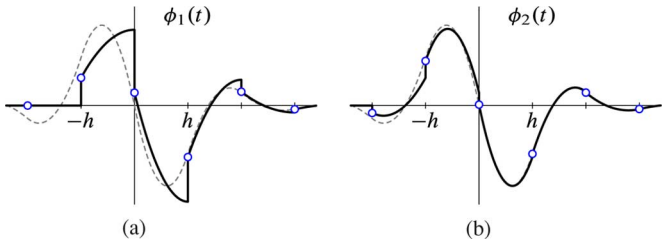

Fig. 10. Interpolation kernels $\phi_l(t)$ for l-causal reconstructing derivative. (a) Smoothing lag $l = 1$, (b) Smoothing lag $l = 2$.

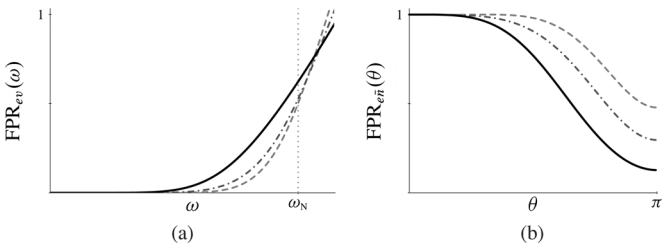

Fig. 11. FPRs with $\Sigma = 0$ (dashed), $\Sigma = 0.006$ (dashed–dotted), and $\Sigma = 0.02$ (solid). (a) Effect of v. (b) Effect of noise.

The optimal performance

$$\mathcal{J}_l = \frac{(3+2\sqrt{3})(1+3\alpha^{2l})}{60}\, h$$

is now proportional to h. The decay rate of $\mathcal{J}_l$ as l increases can be seen from the following table:

l	0	1	2	3
$\mathcal{J}_l/\mathcal{J}_\infty - 1$	3	0.2154	0.0155	0.0011

and is reminiscent of what we saw in the previous example.

D. Effect of Σ

The gain Σ is another, in addition to $\mathcal{G}$, tuning parameter in our design procedure, which can be used to trade off the reconstruction performance and sensitivity to inaccuracies in the acquisition system. In this subsection we examine the effect of this parameter on the properties of the optimal splines in the case of $l = 3$.

The frequency power responses $\mathrm{FPR}_{ev}(\omega)$ and $\mathrm{FPR}_{e\bar{n}}(\theta)$ of the optimal reconstructors for three choices of Σ are depicted in Fig. 11. It is readily seen that the increase of Σ reduces the high-frequency gain of the optimal reconstructor at the expense of a deterioration of the reconstruction performance at frequencies above $\omega_N/2$. At the same time, at low frequencies the effect of Σ is negligible. This can be explained by the interpolation constraint imposed by the poles at the origin in $G_v(s)$, see the discussion at the end of Section V-A. In problems with no interpolation constraints Σ affects the low-frequency range as well.

As mentioned in Section II, discrete noise may represent quantization in an acquisition system (analog noise can be accounted for in the signal generator $\mathcal{G}$). Although quantization is a nonlinear process, it can be analyzed via introducing an additive quantization error, which sometimes may even be well modeled as a white process; see [18, Ch. 20] and the references therein. We may expect that in this case the reconstruction performance may be improved by an appropriate tuning of Σ.

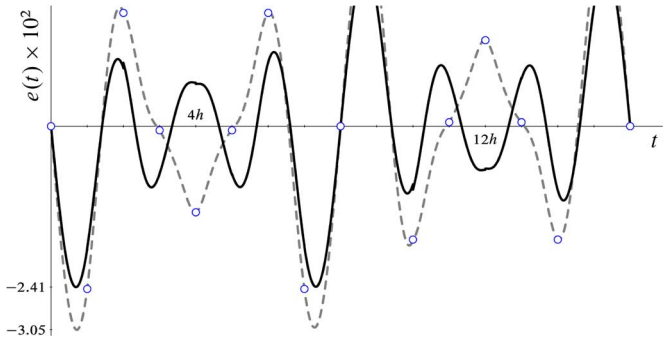

Fig. 12. Reconstructing (29) from 5-bit quantized measurements (dashed line: $\Sigma = 0$ and $P_e = 3.58 \times 10^{-3}$; solid line: $\Sigma = 0.02$ and $P_e = 2.05 \times 10^{-3}$).

To illustrate this point, consider the reconstruction of the bandlimited triangle wave (29) studied in Section V-B. Because this reconstructed signal is periodic, so is the quantization noise and we may again consider properties of the steady-state reconstruction error. Assume that the signal $v(t)$ in (29) is measured via a 5-bit A/D converter in the range $(-1.1, 1.1]$. The measurements are shown by small filled dots in Fig. 8(a). Fig. 12 presents the reconstruction error for two designs. The dashed line corresponds to $\Sigma = 0$, i.e., to the design neglecting the quantization. As this reconstruction is consistent, $u(kh) = \bar{y}[k]$, so the dots in Fig. 12 correspond to the actual quantization noise. The solid line represents the design with $\Sigma = 0.02$, whose FPRs are shown in Fig. 11 by solid lines. We can see that for this quantization the addition of the measurement noise $\bar{n}$ to the problem pays off: the power of the error signal P_e reduces by $\approx 75\%$ and its peak by $\approx 27\%$. Of course, the above example is only a particular realization of the quantization effect and the signal $v(t)$ is not very rich (it has effectively only 5 different magnitude levels). The example, however, does show that in some situations tuning Σ may be advantageous in handling quantization effects. A comprehensive analysis of this phenomenon goes beyond the scope of this paper.

VI. Concluding Remarks

In this paper we have addressed the L^2 optimal design of D/A converters (reconstructors) with causality constraints imposed on them. Closed-form optimal solutions have been presented in terms of state-space realizations of the given signal generators. The solutions are in form of exponential/polynomial splines, which have clear structural properties and recover some known structures when preview length $l \to \infty$. Frequency-domain properties of the reconstruction performance has also been analyzed. State space machinery facilitates both computational and implementational efficiency of the resulted reconstructors.

Some related problems that may be of interest in various applications are the subject of ongoing research. It might, for example, be important to have the possibility to impose FIR constraints on the optimal L^2 reconstructors. The approach presented in this paper cannot handle this situation, so different techniques are required. A preliminary result in this direction is reported in [25]. Another interesting problem is an extension of the approach to the L^∞ performance measure, which can be done using the method of [26]. Unlike noncausal cases, L^∞ so-

lutions do not coincide with L^2 ones when causality constraints are imposed and even possess some qualitatively different properties, see [26].

APPENDIX A
PROOFS

Proof of Proposition 3.2: Denote by $\bar{\mathcal{F}}_{h2}$ the system connecting $\bar{y}$ with $\bar{u}_2$ in Fig. 3. Its transfer function is

$$\begin{aligned}\bar{F}_{h2}(z) &= \bar{F}_{\bar{c},l}(z)(I - z^{-1}C_y\bar{F}_c(z)) \\ &= \bar{F}_{\bar{c},l}(z) - \left(I - z^l\bar{A}_l'\right)\left(z^{-1}I - \bar{A}_1'\right)^{-1} \\ &\quad \times C_y'\left(\Sigma + C_yYC_y'\right)^{-1}C_y(zI - \bar{A}_1)^{-1}\Lambda_{11}YB_\phi.\end{aligned}$$

Substituting

$$C_y'\left(\Sigma + C_yYC_y'\right)^{-1}C_y = z\left(z^{-1}I - \bar{A}_1'\right)X + \bar{A}_1'X(zI - \bar{A}_1),$$

which is a rewritten (10), we end up with

$$\bar{F}_{h2}(z) = (z^l\bar{A}_l' - I)X\bar{F}_c(z) + \bar{F}_{\bar{c}2,l}(z).$$

This completes the proof. ∎

Proof of Lemma 3.3: It is readily seen that $\bar{u}_\delta = \bar{\mathcal{F}}_\delta\bar{y}$, where $\bar{\mathcal{F}}_\delta$ is the discrete system with the transfer function

$$\bar{F}_\delta(z) = (\phi_h(0) - \phi_h(h)z^{-1})\bar{F}(z).$$

Taking into account the equalities

$$\Lambda^{-1} = \begin{bmatrix}\Lambda_{22}' & -\Lambda_{12}' \\ 0 & \Lambda_{11}'\end{bmatrix} \tag{30}$$

and $\Lambda_{22}'Y - \Lambda_{12}' = Y\bar{A}_1'$ [the latter follows from (8) and (9)], we have

$$\phi_h(0) - \phi_h(h)z^{-1} = C_v\left[\,\Lambda_{22}' - z^{-1}I \quad -Y(z^{-1}I - \bar{A}_1')\,\right].$$

Hence,

$$\begin{aligned}\bar{F}_\delta(z) = C_v\big((z\Lambda_{22}' - I)z^{-1}\bar{F}_c(z) \\ -Y(I - z^l\bar{A}_l')B_\phi(I - z^{-1}C_y\bar{F}_c(z))\big).\end{aligned}$$

Now, the transfer function $z^{-1}\bar{F}_c(z)(I - z^{-1}C_y\bar{F}_c(z))^{-1}$ is the positive feedback interconnection of $z^{-1}\bar{F}_c(z)$ and C_y. We therefore have

$$z^{-1}\bar{F}_c(z)(I - z^{-1}C_y\bar{F}_c(z))^{-1} = (zI - \Lambda_{11})^{-1}\Lambda_{11}YB_\phi.$$

Thus,

$$\begin{aligned}\bar{F}_\delta(z) &= C_v\big((z\Lambda_{22}' - I)(zI - \Lambda_{11})^{-1}\Lambda_{11}YB_\phi \\ &\quad -Y(I - z^l\bar{A}_l')B_\phi\big)(I - z^{-1}C_y\bar{F}_c(z)) \\ &= z^lC_vY\bar{A}_l'(I - z^{-1}C_y\bar{F}_c(z))\end{aligned}$$

where the last equality is obtained by $\Lambda_{22}' = \Lambda_{11}^{-1}$. The result then follows by noting that $\bar{\epsilon} = (I - z^{-1}C_y\bar{F}_c(z))\bar{y}$. ∎

We conclude this Appendix with the following result, which is a slight modification of the Van Loan formulas [27].

Lemma A.1: Let E and F be square, then

$$\int_0^h \mathrm{e}^{E(\tau-h)}G\mathrm{e}^{F(\tau-h)}\,\mathrm{d}\tau = \int_0^h \mathrm{e}^{-E\tau}G\mathrm{e}^{-F\tau}\,\mathrm{d}\tau = \Gamma_{12}\Gamma_{22}^{-1}$$

where

$$\begin{bmatrix}\Gamma_{11} & \Gamma_{12} \\ 0 & \Gamma_{22}\end{bmatrix} := \exp\left(\begin{bmatrix}-E & G \\ 0 & F\end{bmatrix}h\right).$$

Proof: The proof follows by considering the integral as the impulse response of the cascade

$$\begin{aligned}&(sI + E)^{-1}G(sI - F)^{-1}\mathrm{e}^{-Fh} \\ &\qquad = \begin{bmatrix}I & 0\end{bmatrix}\left(sI - \begin{bmatrix}-E & G \\ 0 & F\end{bmatrix}\right)^{-1}\begin{bmatrix}0 \\ I\end{bmatrix}\Gamma_{22}^{-1}\end{aligned}$$

sampled at $t = h$. ∎

APPENDIX B
TRUNCATING SINC-INTERPOLATOR

As mentioned in Section I, the main approach to the design of reconstructors with some degree of causality available in the literature is an ad hoc truncation of noncausal interpolation kernels. In this Appendix, we demonstrate that this might lead to unexpected complications. Although this result is not directly related to the technical developments of this paper, it further encourages our study of a rigorous ways of imposing causality constraints.

The sinc-interpolator from the Sampling Theorem is known to have a slow decay [2]. In fact, $\mathrm{sinc}_h(t)$ is not an L^1 function, which means that the sinc-interpolator is not bounded as an $\ell^\infty(\mathbb{Z}) \to L^\infty(\mathbb{R})$ operator [4]. It is then conventional wisdom that truncating the sinc interpolation kernel leads to a substantial performance deterioration. Still, the original sinc interpolator is stable in the $\ell^2(\mathbb{Z}) \to L^2(\mathbb{R})$ sense. A somewhat surprising fact, which to the best of our knowledge has not been reported in the literature yet, is that any half-axis truncation of $\mathrm{sinc}_h(t)$ yields an L^2-unstable D/A converter.

Proposition B.1: The D/A converter with the interpolation kernel $\phi(t) = \mathrm{sinc}_h(t)\mathbb{1}(t-\theta)$ is unbounded as a linear operator $\ell^2(\mathbb{Z}) \to L^2(\mathbb{R})$ for every $\theta \in \mathbb{R}$.

Proof: We only need to prove the statement for $\theta = 0$. The interpolation kernel for any other θ can be viewed as an FIR (i.e., stable) perturbation of the one with $\theta = 0$, which does not affect its stability.

So, assume that $\theta = 0$ and consider the following sequence of unit-energy discrete signals indexed by $\nu \in \mathbb{N}$:

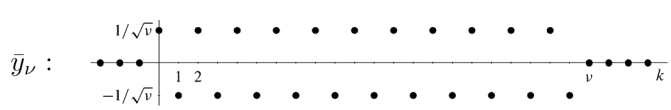

The output of the D/A converter to each of these inputs is

$$u_\nu(kh+\tau) = \frac{(-1)^k \sin(\omega_{\mathrm{N}}\tau)}{\pi\sqrt{\nu}} \sum_{i=\max\{0,k+1-\nu\}}^{k} \frac{1}{i+\tau/h}$$

for all $k \in \mathbb{Z}_0^+$ and $\tau \in [0,h)$. Applying standard harmonic series arguments, the following lower bounds hold:

$$\begin{aligned}|u_\nu(kh+\tau)| &> \frac{|\sin(\omega_{\mathrm{N}}\tau)|}{\pi\sqrt{\nu}} \ln \frac{k+1+\tau/h}{\max\{0,k+1-\nu\}+\tau/h} \\ &> \frac{|\sin(\omega_{\mathrm{N}}\tau)|}{\pi\sqrt{\nu}} \ln \frac{k+2}{\max\{0,k+1-\nu\}+1}.\end{aligned}$$

Thus,

$$\begin{aligned}\|u_\nu\|_2^2 &> \frac{1}{2\pi^2\nu}\left(\sum_{k=2}^{\nu+1} \ln^2 k + \sum_{k=2}^{\infty} \ln^2 \frac{k+\nu}{k}\right) \\ &> \frac{1}{2\pi^2\nu}\sum_{k=2}^{\nu+1} \ln^2 k > \frac{1}{2\pi^2\nu}\int_1^{\nu+1} \ln^2 t\,\mathrm{d}t \\ &= \frac{2+\ln(\nu+1)(\ln(\nu+1)-1)(1+1/\nu)}{2\pi^2}.\end{aligned}$$

Hence, $\|u_\nu\|_2$ grows at least logarithmically with ν. We thus just showed that there is a sequence of unit-energy inputs for which no upper bound on the energy of the output exists. ■

REFERENCES

[1] A. J. Jerri, "The Shannon sampling theorem—Its various extensions and applications: A tutorial review," *Proc. IEEE*, vol. 65, no. 11, pp. 1565–1596, 1977.

[2] M. Unser, "Sampling—50 years after Shannon," *Proc. IEEE*, vol. 88, no. 4, pp. 569–587, 2000.

[3] J. R. Higgins, *Sampling Theory in Fourier and Signal Analysis: Foundations*. Oxford, U.K.: Oxford Univ. Press, 1996.

[4] P. P. Vaidyanathan, "Generalizations of the sampling theorem: Seven decades after Nyquist," *IEEE Trans. Circuits Syst. I*, vol. 48, no. 9, pp. 1094–1109, 2001.

[5] G. Meinsma and L. Mirkin, "Sampling from a system-theoretic viewpoint: Part II—Non-causal solutions," *IEEE Trans. Signal Process.*, vol. 58, no. 7, pp. 3591–3606, 2010.

[6] Y. C. Eldar and M. Unser, "Nonideal sampling and interpolation from noisy observations in shift-invariant spaces," *IEEE Trans. Signal Process.*, vol. 54, no. 7, pp. 2636–2651, 2006.

[7] M. Unser, A. Aldroubi, and M. Eden, "B-spline signal processing: Part I—Theory," *IEEE Trans. Signal Process.*, vol. 41, no. 2, pp. 821–833, 1993.

[8] S. Ramani, D. Van De Ville, T. Blu, and M. Unser, "Nonideal sampling and regularization theory," *IEEE Trans. Signal Process.*, vol. 56, no. 3, pp. 2915–2925, 2008.

[9] D. Petrinović, "Causal cubic splines: Formulations, interpolation properties and implementations," *IEEE Trans. Signal Process.*, vol. 56, no. 11, pp. 5442–5453, 2008.

[10] P. P. Khargonekar and Y. Yamamoto, "Delayed signal reconstruction using sampled-data control," in *Proc. 35th IEEE Conf. Decision Control*, Kobe, Japan, 1996, pp. 1259–1263.

[11] G. Meinsma and L. Mirkin, "Sampling from a system-theoretic viewpoint: Part I—Concepts and tools," *IEEE Trans. Signal Process.*, vol. 58, no. 7, pp. 3578–3590, 2010.

[12] A. H. Jazwinski, *Stochastic Processes and Filtering Theory*. New York: Academic, 1970.

[13] H. M. Robbins, "An extension of Wiener filter theory to partly sampled systems," *IRE Trans. Circuit Theory*, vol. CT-6, pp. 362–370, 1959.

[14] W. Sun, K. M. Nagpal, and P. P. Khargonekar, "H^∞ control and filtering for sampled-data systems," *IEEE Trans. Autom. Control*, vol. 38, no. 8, pp. 1162–1174, 1993.

[15] L. Mirkin and G. Tadmor, "Yet another H^∞ discretization," *IEEE Trans. Autom. Control*, vol. 48, no. 5, pp. 891–894, 2003.

[16] G. Meinsma and L. Mirkin, "Sampled signal reconstruction via H^2 optimization," in *Proc. 2006 IEEE Int. Conf. Acoust., Speech, Signal Process.*, Toulouse, France, 2006, vol. III, pp. 365–368.

[17] G. Meinsma and L. Mirkin, "L^2 sampled signal reconstruction with causality constraints—Part II: Theory," *IEEE Trans. Signal Process.*, vol. 60, no. 5, pp. 2273–2285, 2012.

[18] B. Widrow and I. Kollár, *Quantization Noise: Roundoff Error in Digital Computation, Signal Processing, Control, and Communications*. Cambridge, U.K.: Cambridge Univ. Press, 2008.

[19] T. Kailath, A. H. Sayed, and B. Hassibi, *Linear Estimation*. Upper Saddle River, NJ: Prentice-Hall, 2000.

[20] W. J. Rugh, *Linear System Theory*, 2nd ed. Upper Saddle River, NJ: Prentice-Hall, 1996.

[21] P. Lancaster and L. Rodman, *Algebraic Riccati Equations*. Oxford, U.K.: Clarendon, 1995.

[22] P. Prandoni and M. Vetterli, "From Lagrange to Shannon . . . and back: Another look at sampling," *IEEE Signal Process. Mag.*, vol. 26, no. 5, pp. 138–144, 2009.

[23] Y. Yamamoto and M. Araki, "Frequency responses for sampled-data systems—Their equivalence and relationships," *Linear Algebra Its Appl.*, vol. 205–206, pp. 1319–1339, 1994.

[24] T. Blu and M. Unser, "Approximation error for quasi-interpolators and (multi-)wavelet expansions," *Appl. Comput. Harmon. Anal.*, vol. 6, pp. 219–251, 1999.

[25] Y. Levinson and L. Mirkin, "L^2 signal reconstruction with FIR and steady-state behavior constraints," in *Proc. 50th IEEE Conf. Decision Control*, Orlando, FL, 2011, pp. 7287–7292.

[26] L. Mirkin and G. Tadmor, "On geometric and analytic constraints in the H^∞ fixed-lag smoothing," *IEEE Trans. Autom. Control*, vol. 52, no. 8, pp. 1514–1519, 2007.

[27] C. F. Van Loan, "Computing integrals involving the matrix exponential," *IEEE Trans. Autom. Control*, vol. 23, no. 3, pp. 395–404, 1978.

Gjerrit Meinsma was born in Opeinde, The Netherlands, in 1965. He received the Ph.D. degree at the University of Twente, Enschede, The Netherlands, in 1993.

During the following three years, he held a postdoctoral position at the University of Newcastle, Australia. Since 1997, he has been with the Department of Applied Mathematics at the University of Twente, The Netherlands. His research interests are in mathematical systems and control theory, in particular robust control theory.

Leonid Mirkin (M'99) is a native of Frunze, Kirghiz SSR, Russia (now Bishkek, Kyrgyz Republic). He received the Electrical Engineer degree from Frunze Polytechnic Institute and the Ph.D. (candidate of sciences) degree in automatic control from the Institute of Automation, Academy of Sciences of Kyrgyz Republic, in 1989 and 1992, respectively.

From 1989 to 1993, he was with the Institute of Automation, Academy of Sciences of Kyrgyz Republic. In 1994, he joined the Faculty of Mechanical Engineering at the Technion—Israel Institute of Technology, first as a postdoctoral researcher and then as a faculty member. His research interests include systems theory, control and estimation of sampled-data systems, dead-time compensation, systems with preview, the application of control to electromechanical and optical devices, and robustifying properties of corruption.